

In the format provided by the authors and unedited.

# Wavefront shaping in complex media with a 350 kHz modulator via a 1D-to-2D transform

Omer Tzang<sup>1,3\*</sup>, Eyal Niv<sup>1,3</sup>, Sakshi Singh<sup>1</sup>, Simon Labouesse<sup>1</sup>, Greg Myatt<sup>2</sup> and Rafael Piestun<sup>1</sup>

<sup>1</sup>Department of Electrical, Computer, and Energy Engineering, University of Colorado Boulder, CO, USA. <sup>2</sup>Silicon Light Machines, Sunnyvale, CA, USA.

<sup>3</sup>These authors contributed equally: Omer Tzang, Eyal Niv. \*e-mail: [omer.tzang@colorado.edu](mailto:omer.tzang@colorado.edu)

## Supplementary information

### 1. Theory of 1D-to-2D transform via complex media

In our paper, we show that a 1D phase modulator can be used for controlling light in scattering media since a 1D input gets scattered into a 2D output. Therefore, control of the 1D input can enable control of the 2D output. In the following section we describe this phenomenon rigorously. The relation between the optical fields before and after a scattering sample is represented by the transmission matrix:

$$E_m^{out} = T E_n^{in} = \sum_{n=1}^N t_{mn} E_n^{in} \quad (1)$$

For the 2D case,  $E_n^{in}$  is a vectorized version of the 2D input field and therefore, if the scattering medium is illuminated only on a 1D line we have:

$$E_n^{in} = [0 \quad \dots \quad 0 \quad a_k \quad \dots \quad a_{k+N_{SLM}} \quad 0 \quad \dots \quad 0]^t \quad (2)$$

Even if there are many zeros in the input vector field, none of the output field components can be assumed to be zero:

$$\begin{bmatrix} t_{1,1} & \dots & t_{1,k-1} & & \dots & t_{1,N} \\ \vdots & & \vdots & & & \vdots \\ t_{N,1} & \dots & t_{N,k-1} & & \dots & t_{N,N} \end{bmatrix} T_{1D \rightarrow 2D} \times \begin{bmatrix} 0 \\ \vdots \\ 0 \\ a_k \\ \vdots \\ a_{k+N_{SLM}} \\ 0 \\ \vdots \\ 0 \end{bmatrix} = \begin{bmatrix} E_1^{out} \\ \vdots \\ E_k^{out} \\ \vdots \\ E_N^{out} \end{bmatrix} \quad (3)$$

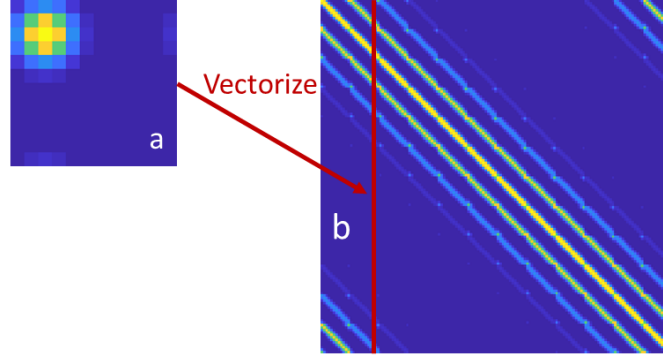
Moreover, the submatrix  $T_{1D \rightarrow 2D}$ , composed of the  $k$  to  $k + N_{SLM}$  columns of  $T$ , represents a linear transformation from the 1D modulated line of the input field to the 2D output field. The elements of the transmission matrix of a scattering sample without memory effect follow the circularly-symmetric complex normal distribution and so do any of the submatrices. This means that  $T_{1D \rightarrow 2D}$  could not be distinguished from a typical 2D transmission matrix. The information of the spatial position of an input mode is lost through the complex medium, in the same way the spatial distribution of the input mode does not affect the statistical properties of the 2D output. This remains true as long as there is no memory effect. Indeed, we show in Fig.2 and Supplementary section 3 that the speckle grain can be elongated in the presence of memory effect.

### 2. Transmission matrix model of scattering medium with memory effect

The transmission matrix representing the linear transformation performed by a complex medium with shift-shift memory effect is simulated by the Hadamard product of two matrices:

$$T_{2D} = S_{2D} \circ G_{2D} \quad (4)$$

where  $S_{2D}$  is a random matrix corresponding to a fully developed speckle field on its columns, and  $G_{2D}$  is a convolution matrix with a circular Gaussian kernel (see Supplementary Fig. 1(a)). The columns of  $G_{2D}$  are composed of vectorized images of a Gaussian kernel, circularly shifted to scan the entire field of view, as depicted in Supplementary Fig. 1. The matrix  $T_{2D}$  is a Block Circulant with Circulant Block (BCCB) matrix and this property can be used to efficiently build the matrix<sup>1</sup>.

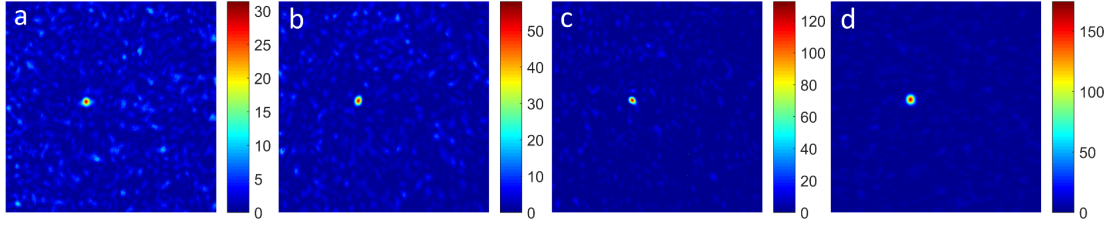


Supplementary Figure 1: **Transmission matrix model of a diffuser with memory effect using a convolution matrix with a Gaussian kernel.** (a) – Circular Gaussian kernel placed at the top left (output coordinate 3,3). (b) Convolution matrix  $G_{2D}$  with a circular Gaussian kernel. The red arrow shows how the vectorized Gaussian kernel (a) is represented by a column in  $G_{2D}$ .

BCCB matrices are fully defined by their first column and can be efficiently built from it. If the input field is represented by an  $N \times N$  image, then  $G_{2D}$  is an  $N^2 \times N^2$  matrix. Let us define the  $N \times N$  submatrices of  $G_{2D}$  as blocks, with indices going from  $1 + N k$  to  $N + N k$  and  $1 + N l$  to  $N + N l$ . The second column of  $G_{2D}$  can be obtained by splitting  $g_1$  into  $N$  parts, each composed of  $N$  pixels, and by a cyclic permutation<sup>1</sup> of each part by one pixel. This operation can be repeated  $N - 1$  times to create the first column of blocks in the matrix  $G_{2D}$  that we define as  $G_1$ . The second column of blocks can be calculated from  $G_1$  by a cyclic permutation of the blocks by one block. The full matrix  $G_{2D}$  is obtained by application of this last operation  $N - 1$  times.

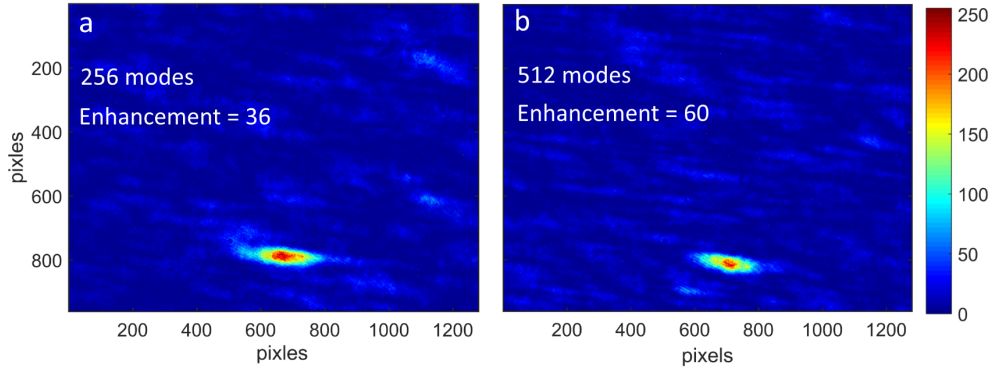
### 3. Speckle shape with 1D illumination

As we describe in Fig. 2 of the main text, the speckle shape at the near-field and far-field may be elongated due to a line (Fourier plane) illumination, depending on the magnitude of the memory effect. For a given memory effect value, the speckle elongation is determined directly by the shape of the illumination on the thin scattering sample. Using a 1D phase modulator and illumination optics that include cylindrical lenses will lead to elongated speckles when the pixels are imaged as elongated stripes, like in our setup, and the scattering sample is placed in or near the Fourier plane. In this case a Fourier transformed illumination of stripes has the shape of orthogonally elongated Fourier components. Moreover, the overlap of the Fourier components generates a line illumination at the input face of the diffuser that forms elongated speckles. In contrast, placing the scattering target at the image plane of the GLV, with an approximate square illumination, generates isotropic, round speckles, even with the extremely large memory effect of a ground glass diffuser. In addition, the presence of astigmatism generates elongated illumination and corresponding elongated speckles in both Fourier and image plane configurations. We highlight the astigmatism aberration since the optical alignment of cylindrical lenses in the GLV setup is sensitive to astigmatism and careful alignment of the tilt angle for each cylindrical lens is required to remove those aberrations. Supplementary Fig. 2 depicts our focusing results when astigmatism was removed, the cylindrical lenses collimation was carefully optimized, and the scattering sample was placed in the image plane of the GLV.



Supplementary Figure 2: **Focusing results with round speckles in image plane illumination configuration.** Real-time focusing using 128 (a) 256 (b) 512(c) and 1024(d) modes. Each image is a snap shot after wavefront optimization. The corresponding enhancements are 30, 37, 62, 74. Experiments performed with a 532nm laser (Coherent Verdi-G).

The enhancement with image plane illumination is comparable to the case of Fourier plane illumination as shown in Supplementary Fig. 3. The figure depicts focusing leading to elongated speckles. The elongation factors of the optimized speckles in Supplementary Figure 3 (a,b) were 3.86 and 2.76 respectively, corresponding to a thin diffuser with  $\sigma = 1.9$  and  $\sigma = 2.7$ .



Supplementary Figure 3: **Focusing with elongated speckles in Fourier plane illumination configuration.** Real-time focusing using 256 (a), and 512 (b) modes. Experiments performed with a 460nm laser (New Focus, Vortex plus TLB 6800).

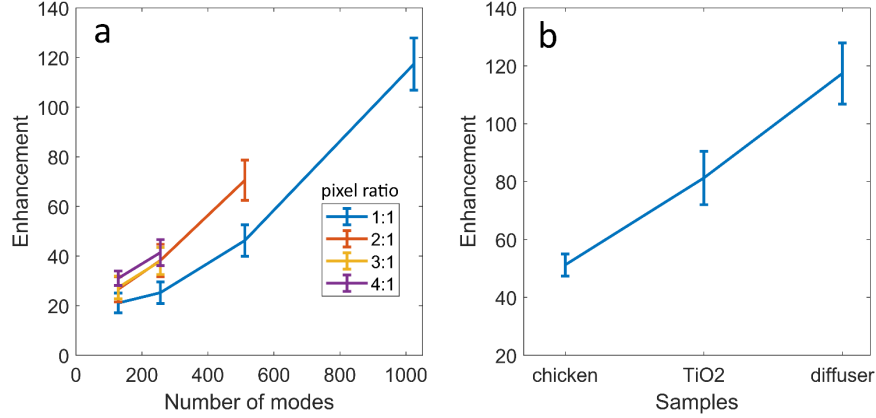
#### 4. Statistical analysis of the enhancement

In the following section we show the performance of our system as a function of several parameters; number of modes, pixel ratio, and scattering sample. For these experiments, we recorded movies of real time focusing through scattering samples while the position of the output speckle field was manually translated with respect to the photodetector, using a mirror.

In the first experiment we focus through a diffuser using different number of Hadamard modes and pixel ratios. The term “pixel ratio” refers to the ratio of GLV pixels to Hadamard mode pixels or the binning of individual GLV pixels. For example, a pixel ratio of 4:1 means that 4 GLV pixels were used to project each Hadamard mode pixel. For the second experiment, we performed focusing through three samples - chicken breast, Titanium dioxide ( $\text{TiO}_2$ ) nanoparticles solution, and a diffuser. The chicken breast was cut into a  $\sim 500 \mu\text{m}$  thick slice and mounted on a microscope slide and the  $\text{TiO}_2$  sample was prepared by diluting  $\text{TiO}_2$  nanoparticles in water and drying it on a microscope slide. The plots in Supplementary Fig. 4(a) and (b), and Fig. 4 (e) of the main paper show the results of the statistical analysis.

In the data processing for both experiments, we selected 500 out of  $\sim 2000$  frames in each movie to report focusing optimizations of speckles with a measurable reference signal, based on the following criteria. First, we removed frames in which the focus was located at the edge of the speckle field because the negligible background beyond the speckle field led to amplified enhancement. These frames were removed by thresholding the deviation of the

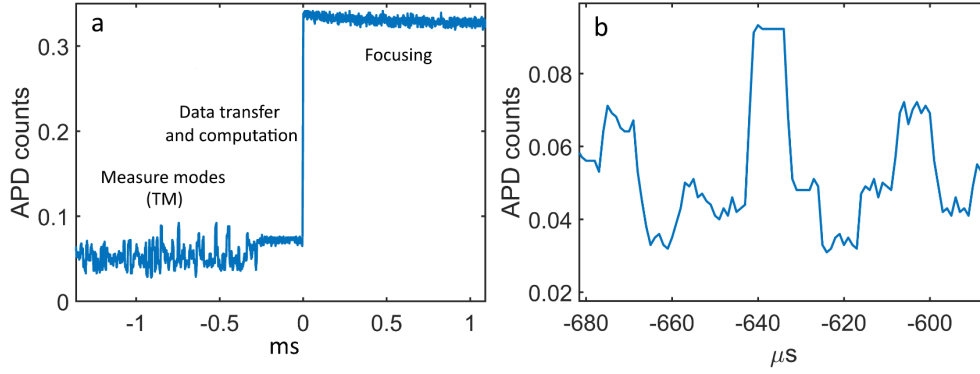
mean pixel value in all the frames. Second, the images where the pre-optimization reference speckle was weak at the desired focus position, typically showed lower enhancement, as can be observed in certain frames in Supplementary movie 1. These frames were removed by thresholding the enhancement value. We also removed pixel noise by median filtering to ensure correct calculation of the enhancement. Finally, we applied a duty cycle correction on the enhancement values to account for the fact that the recorded frames are integrated over both measurement and focusing time. Effectively the statistical analysis represents 500 focusing optimizations of speckle grains overlapping with a measurable reference field.



Supplementary Figure 4: **Performance analysis of the focus enhancement.** (a) Enhancement as a function of the number of modes and pixel ratios. (b) Enhancement for various scattering samples using 1024 modes and pixel ratio of 1:1. Experiments performed with a 532nm laser.

## 5. Processing pipeline for feedback-based computation with maximal GLV bandwidth

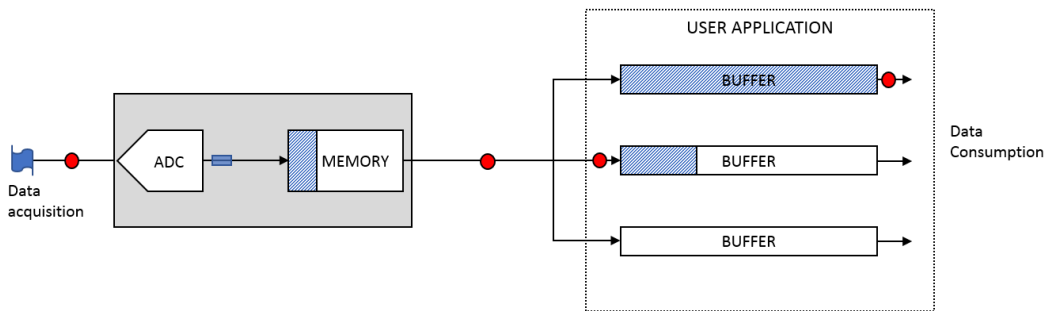
The transmission matrix focusing scheme as well as other adaptive focusing methods, such as genetic algorithms<sup>2-4</sup>, are based on feedback. Depending on the algorithm, additional data processing and computations are required to prepare the focusing wavefront displayed on the SLM. Therefore, besides a high-speed SLM and a fast detector, the key for a high-speed approach is to eliminate any computational, bandwidth, or latency bottlenecks in the feedback loop. While the GLV switches faster than any other available SLM, it is also a very good match for an adaptive, feedback-based application since its electronics was designed to sync data almost as fast as its switching capabilities. The data transfer pipeline to the GLV, in conjunction with its high-speed board (T1088-HS) is sourced over a low latency, high bandwidth, USB3 interface without significantly slowing down the switching rate. Supplementary Fig.5(a) shows the intensity of a feedback speckle during WFS including: several TM measurements, high-speed data transfer and computation, and displaying the calculated phase mask on the GLV for focusing. Supplementary Fig.5(b) shows a detail of the high-speed TM measurements.



Supplementary Figure 5: **High-speed WFS time signals.** (a) Timing of the system: Measured transmission matrix (TM) modes at 350Khz. Transfer data to computer, compute new mask, transfer data to GLV and project: 200  $\mu$ s. Display optimized phase mask: 300 nanoseconds. For 256 modes the TM measurement time is 2.15ms and the real-time focusing cycle is 2.4ms, as depicted in Fig.4. (b) Zoom in of the measured modes (TM), shown in (a). The digitized APD signal shows the intensity of few Hadamard basis modes, each of them interfering with three phase references. Experiments performed with a 460nm laser.

For high speed processing, we utilized the dual-port data acquisition scheme, available in our DAQ, which allows parallelization of data acquisition, data consumption, and processing. The acquired data is captured to an on-board memory buffer, while older data is transferred to the PC simultaneously. Compared to a single port data transfer, the asynchronous data processing scheme, shown in Supplementary Fig. 6, allows continuous real-time monitoring of the signals. A multi-threaded C++ application arms the digitizer to acquire a collection of samples at 500MHz and transfer them directly to the computer memory using Direct Memory Access and without any other copy operations from the CPU. While the digitizer collects the next set of samples, the previous set is processed, and the memory segment is returned to the digitizer memory pool for re-use in the next iteration.

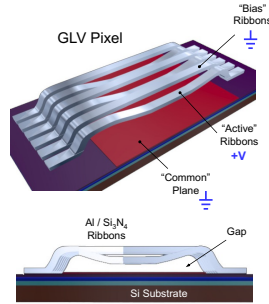
Software data processing included temporal averaging of the digital interference signal, phase calculation, and superposition of the adjusted input modes for generating a focusing vector. Because of the simultaneous nature of the application, the focusing vector was available almost as soon as the data acquisition was completed. The elapsed time from the projection of last input mode to the projection of the focusing vector on the GLV was on the order of 50 $\mu$ s, as depicted in Supplementary Fig.5.



Supplementary Figure 6: **Digital data acquisition and consumption dual-port scheme.** The bounded area indicates a DAQ with Analog-to-Digital Converter (ADC) and on-board memory. Buffers indicate host memory shared between the DAQ and the user application. The data acquisition and data consumption are simultaneous.

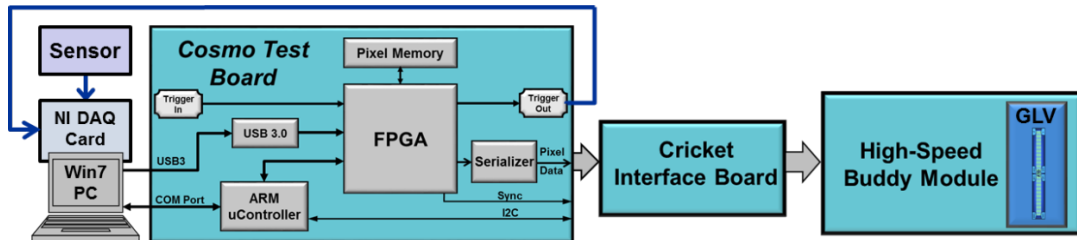
## 6. GLV and Test Board Modifications

The GLV, depicted in Supplementary Fig.7, is a high-speed linear spatial light modulator that is typically used for intensity modulation. Originally, the GLV was composed of 1088 pixels where each pixel comprised of 3 active ribbons and 3 bias ribbons. A modification of the GLV (F1088-P from Silicon Light Machines) provides for phase modulation. The modification converts the bias ribbons into active ribbons so that each pixel comprises 6 active ribbons. The 1088 pixels of the GLV phase modulator implements a phase mask and allows for pure phase modulation in an optical system at an update rate of 350 kHz.



Supplementary Figure 7: GLV Standard Configuration as an Intensity Modulator

The Cosmo Test Board (T1088-HS) is part of the GLV evaluation kit and its function is to write pixel data (i.e. phase masks) to the GLV. Its primary components, depicted in Supplementary Fig.8, are an ARM micro-Controller, FPGA, pixel memory, a USB3 interface for inputting pixel data to the pixel memory and a custom high-speed interface to write the data to the GLV. A sequencer is implemented in the FPGA that writes the pixel data stored in pixel memory to the GLV. The standard configuration of the Cosmo requires that all pixel data is downloaded before starting the sequencer's write operation to the GLV.



Supplementary Figure 8: Cosmo Controller Board driving the Cricket Interface Board and GLV Module

The Cosmo software and FPGA was modified for this application to allow the host computer to write a new line of pixel data via the USB interface into the pixel memory without stopping the sequencer. During system initialization, a group of fixed phase masks are downloaded to the Cosmo pixel memory. During operation the system ran in cycles that consisted of the following steps: Cosmo sequencer writes the group of fixed phase masks to the GLV, the DAQ acquires detector data, a new one-line phase vector is computed by the PC and sent to the Cosmo pixel memory via the USB3 interface and upon receiving the new phase vector, the Cosmo sequencer updates the GLV. The cycle time was greatly accelerated by customizing the Cosmo's firmware and FPGA.

## 7. Phase calibration

Before each set of experiments, we performed offline phase calibration that ensures accuracy in the phase measurements. This calibration step was important since the displacement of the MEMs ribbon with applied voltage is highly nonlinear and the phase modulation with ribbon displacement is wavelength dependent and also sensitive to slight changes of the GLV reflection angle and alignment. During calibration, we displayed a series of phase gratings with increasing voltage on the GLV and recorded the intensity of the zero-order diffraction for each of them. We then fitted the recorded response to simulations. We modeled the GLV as a square phase grating with period  $L$ . The amplitude transmittance of a square phase grating is analytically described as:

$$\begin{aligned} t_A(x) &= 1 - [(1 - e^{j\phi}) \times (\text{square wave})] \\ &= 1 - \left[ (1 - e^{j\phi}) \times \sum_{n=-\infty}^{\infty} c_n e^{j\frac{2\pi nx}{L}} \right] \end{aligned} \quad (5)$$

Where  $c_n$  was defined as the Fourier transform of a rect function:

$$c_n = \frac{1}{L} \int_{-\infty}^{\infty} \text{rect}\left(\frac{\xi}{L/2}\right) e^{-j\frac{2\pi n\xi}{L}} d\xi = \frac{1}{L} F \left\{ \text{rect}\left(\frac{x}{L/2}\right) \right\}_{f_x=n/L} = \frac{1}{2} \text{sinc}\left(\frac{n}{2}\right) \quad (6)$$

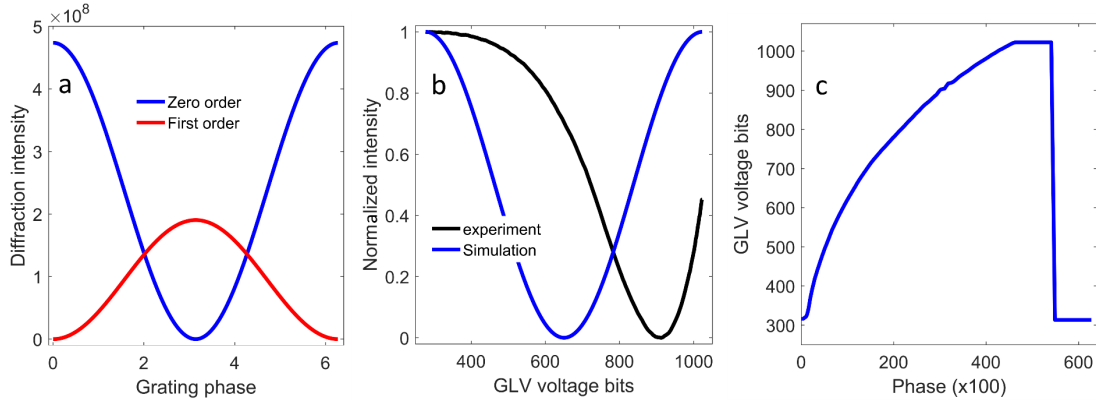
Further, we can Fourier transform the transmission function as:

$$\begin{aligned} F\{t_A(x)\} &= \delta(f_x) - (1 - e^{j\phi}) \sum_{n=-\infty}^{\infty} \frac{1}{2} \text{sinc}\left(\frac{n}{2}\right) F\{e^{j\frac{2\pi nx}{L}}\} \\ &= \delta(f_x) - (1 - e^{j\phi}) \sum_{n=-\infty}^{\infty} \frac{1}{2} \text{sinc}\left(\frac{n}{2}\right) \delta(f_x - \frac{n}{L}) \end{aligned} \quad (7)$$

Using the Fraunhofer approximation, the observed field can be found.

In our calibration, we integrated numerically the Fourier transform of the grating in a spectral region of interest around the zero order and calculated the response as a function of grating phase ramp between  $0 - 2\pi$ , as shown for the 0<sup>th</sup> and 1<sup>st</sup> orders in Supplementary Fig. 9(a). Using the simulation and measurement curves, we then calculated the voltage to phase transformation via tailored offline lookup algorithms that finds the GLV voltage corresponding to a given phase value. In the lookup algorithm, for each  $0 - 2\pi$  phase value, we found the simulated value (y axis in the red curve on Supplementary Fig. 9(b)) and numerically looked for the closest value in the measured curve (y axis in the black curve on Supplementary Fig. 9(b)). The matching x axis values of the two curves accurately map phases to GLV voltages. This calibration lookup table, plotted in Supplementary Fig. 9 (c), was implemented efficiently in our software and allowed high speed operation.





Supplementary Figure 9 : **GLV Phase calibration.** (a) Diffraction efficiency simulation of the GLV. The intensities of the zero and first diffraction orders are plotted in the blue and red curves. (b) Lookup table curves. Black curve – measured and normalized diffraction efficiency of the zero order with GLV gratings. In the measurement, a binary phase grating with values alternating between zero and the ramping GLV-voltage-bits was displayed on the GLV. The intensity of the zero order was measured after a pinhole that blocked all other diffraction orders, using a photodiode. Blue curve- Grating simulation of the zero order, normalized, and symmetrically centered around the black curve. For each phase value and corresponding normalized intensity in the blue curve, the lookup algorithm looks for the voltage values in the black curve that have matching or very close intensities. (c) Plot of the look up table that maps phase to GLV voltage bits. The phase values are multiplied by 100 for efficient software implementation. Note that the GLV's maximal modulation is  $\sim 3\pi/2$  for a wavelength of 460nm, and beyond that, binary voltage values are assigned. The displayed results were obtained with a 460nm laser and we recalibrate the system for each wavelength and alignment configuration.

The alternative calibration method is an interferometric measurement of the GLV phase when ramping up the phase of a plane wave. However, the residual background signal is much stronger than the interference signal and hence, without precise modelling of the background, the signal is buried within the background and the calibration is not applicable.

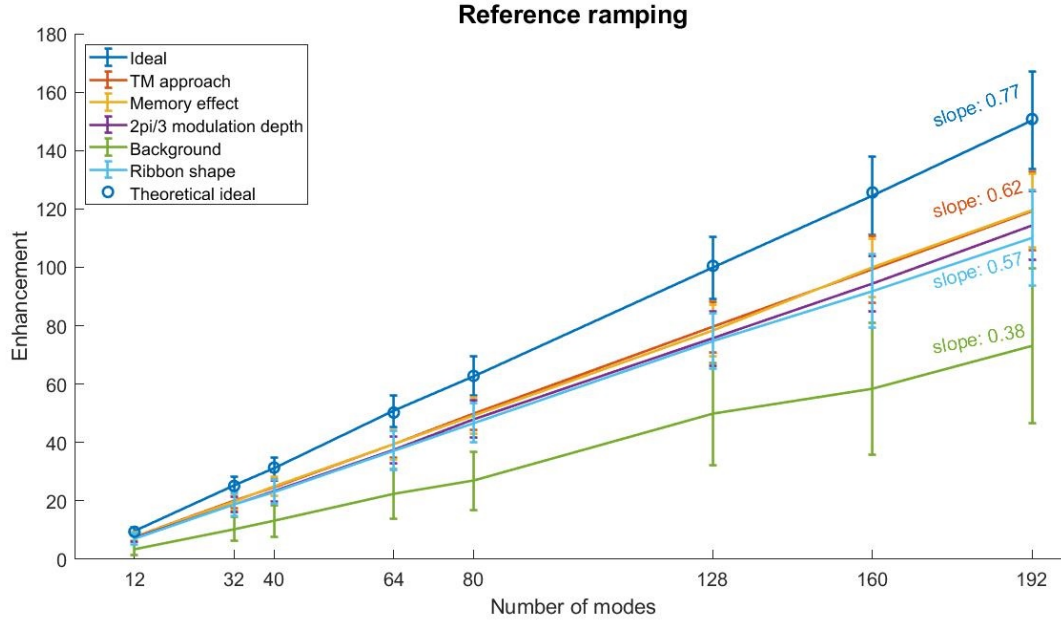
## 8. Characterization and modelling of the GLV performance

The MEMs structure of the GLV and its operation as a phase modulator introduces several effects that reduce the focusing enhancement. In our experiments, the quality of the focused beam is evaluated by the enhancement factor  $\eta$ , which is calculated by dividing the maximum intensity at the focus position by the average value of the surrounding speckle intensities. Theory predicts an average enhancement of  $\eta = (N - 1) \frac{\pi}{4} + 1$ , where  $N$  is the number of input modes, and the wavefront shaping method is phase modulation only<sup>5</sup>. Accordingly, the expected enhancements for  $N = 128, 256, 516$ , and 1024 modes are about 100, 200, 400, and 800 respectively. However, we only observe average enhancements of around 31, 41, 70, and 117 for these values of  $N$ .

In this supplementary section we investigate the differences between the expected and the achieved enhancements, characterize various non-ideal features in simulations and experiments, and determine the significance of each factor.

The simulations of the focusing experiment, performed in MATLAB, considered a GLV with 200 pixels, divided into signal (192 pixels) and reference (8) pixels. The number of Hadamard modes  $N$  for a given simulation was equal to the number of signal pixels. Transmission through the scattering medium was simulated using the transmission matrix approach, described in Supplementary section 2. At the output, a single pixel of the output image simulated the experimental photodetector behind a pinhole. In each simulation, we introduced GLV non-ideal structures and imperfections and calculated the enhancements. Supplementary Fig.10 depicts the investigation of five issues; the use of a fast transmission matrix approach, memory effect, incomplete modulation depth, presence of background light, and imperfect

modulation due to the GLV ribbon shape. Each point in the curves represents the average enhancement value of 200 simulations with different scattering media.



Supplementary Figure 10: **Simulation of the enhancement vs the number of modes with GLV non-ideal structures.** Each curve shows simulations of a different wavefront modulation issue. The error bars are the standard deviation of 200 simulations. Note the enhancement reduction with background (green) while Memory effect (yellow), pixel shape (blue), and modulation depth (purple) have a minor effect on enhancement. The maximal number of modes in the simulation was limited to 192 due to constraints of the Hadamard function in Matlab and for speeding up the calculations.

The first blue curve shows the “ideal” case<sup>6</sup>. This curve fits well with the theory as shown by the blue circles. Indeed, with no memory effect, the spatial arrangement of the pixels does not affect the enhancement. In our experiments and in all the remaining simulations, we used a TM approach with Hadamard input modes and phase-only modulation. Our simulations show a  $\sim 20\%$  decrease of the enhancement compared to the ideal case. According to Supplementary Fig.10, the most significant effect that reduces the enhancement is “background” while the other investigated effects (Memory effect, shape of the GLV ribbons, and depth of modulation) are less significant. In what follows, we describe the non-ideal features one by one, characterize them, and explain how we simulated them in Supplementary Fig.10. Note that the simulated enhancements correspond to each isolated non-ideal aspect of the GLV and hence they are not supposed to match the experiment which is affected by a combination of these factors.

### 8.1. Memory effect

The presence of memory effect in thin scattering samples may change the speckles’ shape when the sample illumination is shaped as a line (Fourier plane illumination), as we explain in Fig. 2 of the main text. Here, we test in simulations whether the anisotropic shape of speckles reduces the WFS control. The memory effect is simulated by keeping only one line of the simulated TM, as explained in Fig. 2 and Supplementary Sec. 2. The simulation results in the yellow curve of Supplementary Fig. 10 show that the presence of memory effect does not reduce the enhancement and WFS control with respect to the TM with isotropic speckles. This is a non-intuitive insight explained by the observation that each pixel of the GLV generates a speckle pattern that can be phase controlled to interfere constructively. The achievable intensity at the focus is not reduced due to the particular shape of the speckle.

In our experiments, we can tune the speckle elongation, for example by controlling the beam astigmatism by rotation of the cylindrical lens. In agreement with simulation, we see no experimental evidence that the enhancement reduces with speckle elongation.

## 8.2. Modulation depth

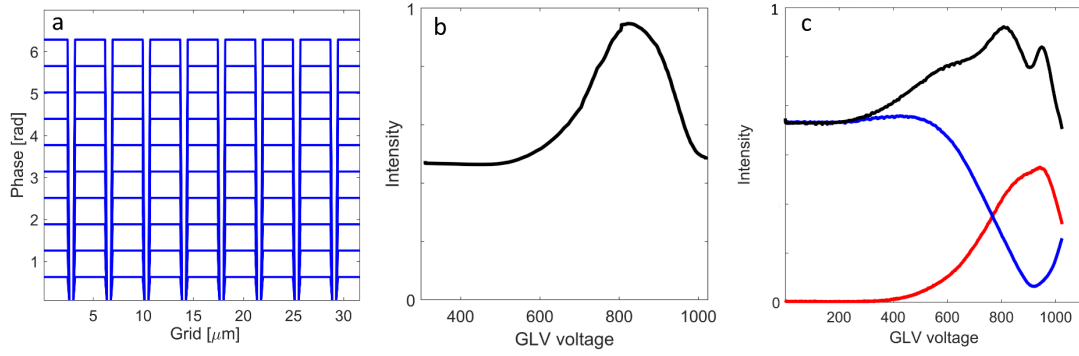
In WFS, controlling the phase of the illumination continuously over the complete  $2\pi$  range is desired for optimal control. The phase modulation range, determined by the GLV ribbon displacement, reached only  $\sim 3/2\pi$  with our 460nm laser, which matches 400nm at a reflection angle of 0 degrees. This incomplete modulation depth was caused by a mismatch in the tested GLV device to the wavelength of the laser. As a result, all phases between  $3/2\pi$ - $7/4\pi$  were set to  $3/2\pi$  and all phases between  $7/4\pi$ - $2\pi$  were set to  $2\pi$ . Using a longer wavelength of 532 nm reduced the modulation depth even further. This limited phase range reduces the accuracy of the calculated phase-conjugated wavefront. To test this effect, we simulated the modulation depth by setting the phase values that are beyond the modulation depth to the closest accessible phase. The purple curve in Supplementary Fig. 10 shows that the limited modulation depth had a relatively minor effect on the enhancement. Moreover, we found that the enhancement ( $\eta$ ) of ideal WFS with a modulation depth  $a$ , where  $a$  is defined as a fraction of  $2\pi$ , can be analytically predicted to be,

$$\eta(a) = \left( \frac{\sin(a/2)}{\pi} + \frac{a}{2\pi} \right)^2 \times \eta \quad (8)$$

The mean intensity before focusing is not affected by incomplete phase modulation. However incomplete phase modulation prevents the alignment of all the output modes and reduces the focus intensity. Supplementary Eq. 8 shows that  $\eta(3\pi/2) = 0.95\eta$ . Hence, the enhancement is close to the ideal  $\eta$  for modulation depth larger than  $3\pi/2$ . Note that the GLV used in the experiments was an off-the-shelf device and was not optimized for the 460 nm laser. It is possible to develop a customized GLV device that could provide the full  $2\pi$  phase shift for different wavelengths.

## 8.3. Background modulation signal

Each GLV pixel consists of six ribbons, each  $\sim 3.75\mu\text{m}$  wide with gaps of  $\sim 0.5\mu\text{m}$  between them. This inter-ribbon gap structure essentially forms a high spatial frequency grating along the device. In WFS, ramping up a constant phase along a group of pixels modifies the phase of the wave. When ramping up phase with the GLV, the efficiency of the inter-pixel grating changes and as a result, a modulated plane wave experiences a residual intensity modulation that we denote as the background signal. This background modulation signal interferes with the phase measurement for focusing and may distort measurements of spatial modes, especially for modes that produce weaker speckles on the detector. Supplementary Fig. 11 depicts a comparison of simulation and measurement of the background signal. In the simulation, we ramp up all the GLV pixels across their full phase range of 0 to  $2\pi$ , as depicted in Supplementary Fig. 11(a), calculate numerically the diffraction efficiency at the zero order, and plot the intensity as a function of the GLV voltage (calibrated ramping phases) in Supplementary Fig. 11(b). We do not know precisely the distance between the back-reflecting surface and the position of the ribbons at zero GLV voltage. Therefore, we tuned the simulation with a (free parameter) distance (phase shifts of  $\pi$ ) to approximate the measurements. The characterization experiment is shown in Supplementary Fig. 11(c). The measured signal, depicted in the black curve, has a different shape and includes additional modulation features compared to the simulation. We also show the experimental zero (blue) and first order (red) diffraction efficiency curves for comparison. These curves were measured by ramping a pixel grating from 0 to the maximal GLV voltage, where all even pixels were fixed to zero GLV voltage.



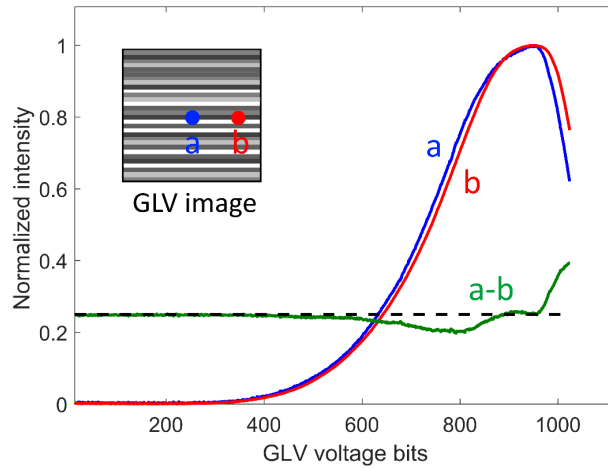
Supplementary Figure 11: **Residual background modulation due to the GLV's inter-pixel gaps.** a- Simulation of the GLV grating with its ribbons moving up and down, corresponding to phase modulation between 0 and  $2\pi$ . b – Simulated diffraction efficiency of the zero order as a result of the GLV ribbons modulation. We added a  $\pi$  phase shift to the simulated grating to account for the distance of the ribbon from the back-reflecting surface of the device. c- Experimental characterization of the GLV grating with its ribbons moving up and down. Black- the zeroth order diffraction measured with pixel ramping and normalized. All the pixels (and ribbons) are moving up and down to measure the background signal. Blue- the zeroth order diffraction, measured with a pixel grating, namely every second pixel is fixed, and the remaining pixels are moving up and down, forming a high efficiency grating. Red- the first order diffraction with pixel grating. The ribbons move up to the maximal GLV voltage and do not reach  $2\pi$ , as described previously. Experiments performed with a 532nm laser.

A comparison of the simulated black curve in Supplementary Fig. 11(b) and the experimental black curve in Supplementary Fig. 11(c) shows two main differences. First, the simulated background trend does not match precisely the experiment. This may be explained by a phase wrapping effect. The distance to the back surface of the GLV is unknown and hence in the simulation we adjusted a distance, that is equivalent to a  $\pi$  phase shift, to match the simulation trend with the experiment, but there is no guarantee that this phase shift is precise. Second, the black curve in Supplementary Fig. 11(c) shows multiple oscillations. This effect may be explained by the interference of multiple reflections in the GLV device due to the angular illumination. The inter-pixel gaps may transmit multiple-reflections from the back surface of the GLV MEMS chip that interfere with the modulated signal and further complicates the modelling of the GLV. The presence of background signal, composed of a combination of grating and interference effects not only complicates the modelling of the GLV but also directly distorts the phase calibration procedure that relies on modelling the GLV as a square grating, as described in the Supplementary Sec. 7. The resulting phase error in the TM measurement and phase conjugation translates directly to reduced enhancement when focusing.

To simulate a simplified background signal and calculate its effect on the enhancement, a fraction of the GLV pixels was kept constant. The pixels were composed of  $P = 3$  ribbons and only two ribbons are set to the desired phase while the last ribbon acts as a fixed reflecting surface, generating a background signal. Our simulation, depicted in the green curve of Supplementary Fig. 10, shows that the enhancement reduces by 40% due to this effect.

#### 8.4. Ribbon shape - non-uniform bending of the MEMS ribbons along each pixel

The bending mechanics of the MEMS ribbons generate a non-uniform surface with varying phase delays along the pixel. To characterize this effect, we sampled a magnified image of the ribbon at different locations and measured the diffraction efficiency of the first order. Our optical setup, including a re-collimating cylindrical lens after the GLV, forms an image of the GLV where the pixels are extended to stripes along the horizontal axis, as shown in the top left inset of Supplementary Fig. 12. Hence, this allows probing the diffraction efficiency by placing a small detector and translating it along the image of the ribbon. This measurement shows qualitatively how phase modulation varies along the pixel.



Supplementary Figure 12: **Measurement of first-order diffraction at various locations (a, and b) along the GLV elongated pixels.** We image the GLV and translate a photodetector along the pixel while displaying gratings with increasing voltages (phase differences) on the GLV. In this experiment, the wavelength of the laser was 532nm and hence the maximal modulation is lower than the modulation depicted in Supplementary Fig.5, where we used a 460nm laser. Note the difference signal (a-b) and lower modulation depth at the sides of the pixel due to non-uniform bending mechanics of the GLV ribbons. Experiments performed with a 532nm laser.

The effect of non-uniform bending can be minimized by tightly focusing the beam on the GLV using a short focal length cylindrical lens. We found that using a 100mm cylindrical lens is optimal for our configuration, in terms of reflection geometry, while still producing a tight beam. We measured the focused beam size at the GLV to be  $10\mu\text{m}$  and it is much smaller than the ribbon size,  $220\mu\text{m}$ .

To simulate the effect of the ribbon shape on the enhancement, we assume a simplified geometry where two ribbons of the pixel are set to the desired phase and one is set to  $7/8$  of the correct phase, generating a systematic phase error. This model represents the effect of a nonuniform GLV ribbon where the phase at the center of the ribbon is well defined, however geometrical nonuniformity along the ribbon generates increasing phase errors for off-center reflected light. The magnitude of the phase error in our simulation was estimated based on the characterization experiment shown in Supplementary Fig.12. As seen in the light-blue curve in Supplementary Fig.10, the bending of the pixel causes a 7.7% reduction in the enhancement that is much lower than the background effect, previously described. The effect of nonuniform bending of ribbons depends on the beam to ribbon width ratio, and the actual shape of the ribbons in dynamic operation of the GLV.

## References

1. Davis, P. J. *Circulant matrices*. (American Mathematical Soc, 2012).
2. Conkey, D. B., Brown, A. N., Caravaca-Aguirre, A. M. & Piestun, R. Genetic algorithm optimization for focusing through turbid media in noisy environments. *Opt. Express* **20**, 4840 (2012).
3. Tzang, O., Niv, E., Caravaca-Aguirre, A. M. & Piestun, R. Thermal expansion feedback for wave-front shaping. *Opt. Express* **25**, 6122 (2017).
4. Tzang, O. & Piestun, R. Lock-in detection of photoacoustic feedback signal for focusing through scattering media using wave-front shaping. *Opt. Express* **24**, 28122 (2016).
5. Vellekoop, I. M. Feedback-based wavefront shaping. *Opt. Express* **23**, 12189 (2015).
6. Popoff, S. M., Lerosey, G., Fink, M., Boccarda, A. C. & Gigan, S. Controlling light through optical disordered media: Transmission matrix approach. *New J. Phys.* **13**, (2011).